

1      **Synthesis of  $\text{Fe}_3\text{O}_4$ /  $\text{ZnO}/\text{CuO}$  Nanocomposite and its Sono-**  
2      **photocatalyst property for removal of methylene blue from**  
3      **wastewater**

4

5      **Samira Pishkar Ahrab<sup>1</sup>, Mahdiyeh pourali<sup>2</sup>, MohammadTaghi Hamedani<sup>\*1</sup>,**

6

7      1. Faculty of Mechanical Engineering, Tabriz University, Tabriz, 51616471, Iran.

8      2. Faculty of Materials Engineering, Sahand University of Technology, Tabriz, 513351996, Iran.

9

## 10     **Abstract**

11      $\text{Fe}_3\text{O}_4/\text{ZnO}/\text{CuO}$  nanocomposites with various molar ratios of  $\text{CuO}$  were successfully synthesized. Sol-  
12     gel method was used to synthesize nanocomposite materials at a low temperature. A set of experiments,  
13     including X-ray diffraction (XRD), Dynamic Light Scattering (DLS), scanning electron microscopy  
14     (SEM), and UV-Vis spectroscopy, was used to confirm the successful synthesis of  $\text{Fe}_3\text{O}_4/\text{ZnO}/\text{CuO}$   
15     nanocomposites in crystalline form.

16     The photocatalytic activity of the samples was investigated via the degradation of methylene blue (MB)  
17     dye from synthetic wastewater under three distinct conditions: visible light, ultraviolet light, and a  
18     combination of visible light with ultrasonic treatment.  $\text{Fe}_3\text{O}_4/\text{ZnO}/\text{CuO}$  nanocomposite with a molar ratio  
19     of 1:1:0.5 showed the highest photocatalytic activity when irradiated with either visible or ultraviolet light.  
20     Furthermore, when visible light was combined with ultrasonic treatment, complete (100%) removal of  
21     methylene blue was achieved within 120 minutes. The results demonstrate that these nanocomposites are  
22     efficient catalysts for wastewater treatment through the removal of organic pollutants.

23

24     **Keywords**  $\text{Fe}_3\text{O}_4/\text{ZnO}/\text{CuO}$ , Sono-photocatalyst, nanocomposite, Wastewater treatment

25

26

## 27     **1 Introduction**

28     Over the past few decades, there have been  
29     some emerging problems in the industry,  
30     whereas environmental pollution has attracted  
31     a lot of attention in the world [1]. The release  
32     of organic dyes from the textile, leather, food,  
33     cosmetics, and pharmaceutical industries into  
34     the environment has resulted in significant  
35     issues for living organisms. Also, water  
36     pollution is a problem that should be identified  
37     as soon as possible. Researchers have done a  
38     great deal of research on how to treat infected  
39     water from the processing of industrial  
40     products and household waste [2].

41     Nevertheless, the conventional wastewater  
42     treatment method still contains a large number  
43     of contaminants that are challenging to  
44     eliminate. For instance, antibiotics, dyes,  
45     organic insecticides, multi-rheological  
46     aromatic hydrocarbons [3-6], etc. New  
47     techniques, like Fenton oxidation [7] and a  
48     hybrid approach that combines multiple  
49     purification processes, like active carbon,  
50     biofilm, enzymatic reactors, etc., have been  
51     developed to remove these contaminants [8].  
52     These techniques have garnered interest from  
53     researchers [9] and have a positive impact on  
54     the degradation of contaminated organic  
55     matter. Another method for removing

---

\* Corresponding author

Professor of Materials science and engineering, Mechanic faculty, Tabriz university, Tabriz ,Iran.

Email [m.hamedani.tabrizu@gmail.com](mailto:m.hamedani.tabrizu@gmail.com), Tel: +989147618082 & +98-41-33356026, Fax: +98-41-33354153

56 pollutants is to use Semiconducting oxides with  
57 photocatalytic properties. Various catalysts  
58 have been introduced to remove pollutants or  
59 even make them non-irritating chemicals [10].  
60 Among them,  $\text{TiO}_2$  and  $\text{ZnO}$  semiconductors  
61 have been introduced as successful  
62 photocatalysts for the destruction of organic  
63 pollutants. The advantages of  $\text{ZnO}$   
64 nanoparticles include strong oxidizing ability,  
65 light sensitivity, excellent mechanical and  
66 chemical stability, non-toxic nature, favorable  
67 energy gap, and cheap price [11]. However, to  
68 use  $\text{ZnO}$  as a photocatalyst, according to the  
69 band gap (3.2 electron volts), it is necessary to  
70 use ultraviolet light that only contains less than  
71 10% of the sun's light. While in the sunlight,  
72 45% of the radiation is visible in the lightrange  
73 [12,13]. To enhance the photocatalytic activity  
74 of  $\text{ZnO}$  under the influence of visible light,  
75 solutions need to be considered. The formation  
76 of a  $\text{ZnO}$  nanoparticle composite with other  
77 metal oxides results in the absorption of  
78 stronger light and increased ability to absorb  
79 visible light [14]. In addition, this composite  
80 prevents recombining electron-hole and  
81 increases the photocatalyst's efficiency [15].  
82 The coupling of  $\text{ZnO}$  with  $\text{CuO}$  nanoparticles  
83 and their composite formation is a promising  
84 method for increasing photocatalytic  
85 properties. Besides extending the absorption  
86 range towards the visible light, this method  
87 transmits electrons produced by the photon  
88 from a high-conductivity band of  $\text{CuO}$  to a low-  
89 conductivity band of  $\text{ZnO}$ , which results in the  
90 effective separation of the electron-hole [16].  
91 So far, considerable research has been done on  
92 the synthesis of  $\text{ZnO} / \text{CuO}$  as a special high-  
93 level catalyst. Number of techniques have been  
94 put up to create a  $\text{ZnO}/\text{CuO}$  catalyst, such as  
95 mechanical methods, for example grinding wet  
96 chemistry, coprecipitation, thermal  
97 decomposition, sol-gel, hydrothermal, and  
98 photo deposition methods [17]. Another  
99 problem for catalysts is their segregation from  
100 purified water in practical applications.  
101 Traditional methods such as coagulation and  
102 filtration cause catalyst degradation and  
103 increase energy consumption [18]. Using an  
104 external magnet, researchers have recently  
105 paired magnetic nanoparticles with

106 photocatalytically active materials to improve  
107 catalyst separation and recycling [19].  
108 Therefore, the introduction of magnetic  
109 materials such as  $\text{Fe}_3\text{O}_4$  in  $\text{Fe}_3\text{O}_4/\text{ZnO}/\text{CuO}$   
110 nanocomposites simplifies the magnetic  
111 separation. Nanocatalysts are beneficial for  
112 academic and industrial research due to their  
113 high reaction rates, perfect activation of  
114 adsorbed compounds, ease of use, high  
115 selectivity, recyclability, and eco-friendliness.  
116 Because of their appealing features, nanometal  
117 oxides have been utilized as solid catalysts in a  
118 variety of organic processes [20].  
119 In explaining the photocatalytic effect, it can be  
120 said that in the absence of degradation matter,  
121 hydrocarbons often decompose slowly.  
122 Photocatalyst reduces the activation energy of  
123 the decomposition process and therefore,  
124 accelerates the reaction. As a result of the light  
125 collision with photocatalytic materials,  
126 electron holes create high oxidation and  
127 resuscitation [21].  
128 Nowadays, the use of ultrasonics in the  
129 presence of a catalyst (sonocatalytic  
130 decomposition) is an eco-friendly method for  
131 removing dyes from wastewater. The influence  
132 of ultrasonic waves is the heat produced by a  
133 hole explosion, which converts water  
134 molecules into hydroxyl radicals and reactive  
135 hydrogen atoms. Both species can react with  
136 organic dyes, which can lead to the breakdown  
137 and elimination of different contaminants from  
138 wastewater[22].  
139 As a result, the simultaneous use of light and  
140 ultrasonic radiation to analyze different colors  
141 has been investigated [19-22].  
142 In the current study, the impact of light and  
143 ultrasound irradiation and the metal oxide  
144 content has been investigated on the  
145 photocatalytic activity of the  $\text{Fe}_3\text{O}_4/\text{ZnO}/\text{CuO}$   
146 nanocomposites. The optical and  
147 morphological analysis proceeded with a  
148 photocatalytic activity test in methylene blue  
149 (MB) degradation from wastewater.  
150

151 **2 EXPERIMENTAL PROCEDURES**

152

153 In this study Iron (II) sulfate heptahydrate  
154 ( $\text{FeSO}_4 \cdot 7\text{H}_2\text{O}$ , 99%), copper sulfate  
155 pentahydrate ( $\text{CuSO}_4 \cdot 5\text{H}_2\text{O}$ , 99%), zinc sulfate

156 heptahydrate ( $\text{ZnSO}_4 \cdot 7\text{H}_2\text{O}$ , 99%) and sodium  
157 hydroxide (NaOH) (Merck Company) was  
158 used as raw materials.

159  $\text{CuO}$  and  $\text{Fe}_3\text{O}_4$  nanoparticles were synthesized  
160 using the sol-gel method. In this method, 0.025  
161 mole of  $\text{CuSO}_4 \cdot 5\text{H}_2\text{O}$  was dissolved in 100 mL  
162 of deionized water with constant magnetic  
163 stirring. Then 0.05 mole of NaOH was  
164 dissolved in 150 mL of deionized water and  
165 added to the solution in a droplet form to obtain  
166 the appropriate pH. The solution was then  
167 maintained at  $80^\circ\text{C}$  for 3 hours to form the gel.  
168 After 4 hours, the black product was dissolved  
169 using filter paper and dried at  $80^\circ\text{C}$  for 4 hours  
170 in an oven to achieve Copper oxide  
171 nanoparticles.

172 To obtain  $\text{Fe}_3\text{O}_4$  nanoparticles, 0.027 mole of  
173  $\text{FeSO}_4 \cdot 7\text{H}_2\text{O}$ , dissolved in 100 mL of deionized  
174 water and continuously stirred at room  
175 temperature. To control the pH in 3, acetic acid  
176 ( $\text{CH}_3\text{COOH}$ ) and 30 mL of ethylene glycol  
177 (EG), both of them in pure form, were added to  
178 the solution. Then, 0.054 mole of NaOH was  
179 dissolved in 150 mL of deionized water and  
180 added dropwise to the mixture. The final  
181 solution was stirred at  $80^\circ\text{C}$  for 3 h to form a  
182 gel. The gel was dried at  $80^\circ\text{C}$  for 4 h.  
183 To synthesize the  $\text{Fe}_3\text{O}_4/\text{ZnO}/\text{CuO}$   
184 nanocomposite, 0.0125 mole of  $\text{ZnSO}_4 \cdot 7\text{H}_2\text{O}$   
185 was dissolved in 30 mL of distilled water with  
186 magnetic stirring. Then, 0.025 mole of NaOH  
187 in 65 mL of deionized water was added to the  
188 solution in droplets to reach the appropriate  
189 PH, which was then stirred and heated at  $80^\circ\text{C}$ .  
190 The previously synthesized  $\text{Fe}_3\text{O}_4$  and  $\text{CuO}$   
191 nanoparticles were dispersed in 30 mL of  
192 ethanol (99.7%) and then added to the initial  
193 solution. The resulting mixture was  
194 continuously stirred at  $80^\circ\text{C}$  for 2 hours.  
195 Finally,  $\text{ZnO}$  was formed in situ on the surface  
196 of the pre-formed  $\text{Fe}_3\text{O}_4$  and  $\text{CuO}$ . At the end  
197 the product was isolated using filter paper and  
198 washed several times with distilled water and  
199 ethanol to remove impurities. The final product  
200 was left at room temperature overnight and  
201 dried at  $100^\circ\text{C}$  for 1 hour. Nanocomposite  
202  $\text{Fe}_3\text{O}_4/\text{ZnO}/\text{CuO}$  with the molar ratios of  
203 (1:1:0.3, 1:1:0.5, 1:1:1, 1:1:3) was prepared by  
204 changing the concentrations of the precursor  
205 solutions and evaluated.

206 X-ray diffraction peaks were measured by an  
207 XRD analyzer (Siemens D5000 X-ray  
208 diffractometer). The analysis was conducted  
209 under the conditions of  $\text{Cu-}\kappa\alpha$  radiation  
210 ( $\lambda=1.54178\text{\AA}$ ), a scanning rate of  $20^\circ/\text{min}$ , a 20  
211 range of  $20$ – $80^\circ$ , and operating conditions of 30  
212 kV and 40 mA. Also, Crystallite size is  
213 estimated by Scherer's equation (Eq.1) [23]:  
214  $D=0.9\lambda/\beta\cos\Theta$  (Eq. 1)

215 where  $D$  is the size of the crystals in  
216 nanometers,  $\beta$  is the peak width at half the  
217 maximum intensity in radians in radian,  $\lambda$  is the  
218 x-ray wavelength in nanometers, and  $\Theta$  is the  
219 Bragg angle corresponding to the diffraction  
220 peak.

221 SEM (Stereo Scan 360) was conducted to  
222 verify the morphology of the obtained  
223 nanoparticles. Elemental analysis of the  
224 samples was performed using X-ray diffraction  
225 spectroscopy (EDX). A dot map was used to  
226 determine the distribution of the elements in the  
227 nanocomposite. To investigate particle size  
228 distribution from DLS, Nanotrac Wave of  
229 Micro trac Co. was used and to determine the  
230 adsorption edge and band gap of synthesized  
231 zinc oxide and prepared nanocomposites, DRS  
232 spectroscopic analysis was performed. The  
233 absorption wavelength was obtained by  
234 extrapolating the linear part of the absorption  
235 intensity curve in terms of wavelength.

236 Eq. 2 was used to calculate the band gap [24]:  
237  $Eg = hc / \lambda g$  (Eq. 2)

238 In this respect,  $Eg$  is the band gap in electron  
239 volts,  $h$  is the Planck constant equals  
240  $4.13567 \times 10^{-15}$  ev,  $c$  is the light speed equals  
241  $299792458$  m / s and  $\lambda g$  is the absorption  
242 wavelength.

243 The effectiveness of the photocatalysts was  
244 tested by measuring their ability to break down  
245 methylene blue (MB) in 100 mL beakers. In  
246 this test, the UV-C Philips 9W lamp was used  
247 as UV light and the 120-watt metal halide lamp  
248 was used as a visible light source. A  
249 photocatalytic test equipment was mounted and  
250 sealed in a dark chamber to prevent the loss of  
251 radiation. For the determination of  
252 photocatalytic activity, 0.05 g of the  
253 nanocomposite samples was dispersed in 100  
254 ml of MB solution with a concentration of  
255 0.005 g / l using a magnetic stirrer.  
256 Before illumination, the reaction mixture was

257 kept in dark conditions for 20 minutes to  
 258 establish adsorption-desorption equilibrium.  
 259 After collecting the initial sample, the  
 260 photocatalytic reaction was initiated by  
 261 activating the light source. Subsequent samples  
 262 were collected at 20-minute intervals  
 263 (specifically at 20, 40, 60, 80, 100, and 120  
 264 minutes), and each sample underwent UV-Vis  
 265 spectroscopic analysis. The concentration of  
 266 Methylene Blue (MB) was determined by  
 267 measuring the UV-Vis absorbance at its  
 268 characteristic peak wavelength of 665 nm. A  
 269 calibration curve was created and used to  
 270 convert the measured absorbance values into  
 271 actual dye concentrations. The degradation rate  
 272 was then determined using the following  
 273 equation [25]:  
 274

$$275 \quad (I_0 - I_t)/I_0 \times 100 = (C_0 - C_t)/C_0 \times 100 \quad (\text{Eq. 3})$$

276  
 277 Where C represents the concentration of  
 278 Methylene Blue (MB) at any given time during  
 279 the reaction, while C<sub>0</sub> is the initial MB  
 280 concentration after reaching adsorption-  
 281 desorption equilibrium, similarly, A represents  
 282 the absorbance value measured at any point  
 283 during the reaction, and A<sub>0</sub> is the initial  
 284 absorbance value recorded at equilibrium.  
 285 To evaluate how ultrasonic treatment affects  
 286 photocatalytic activity, Fe<sub>3</sub>O<sub>4</sub>/ZnO/CuO  
 287 nanocomposites (0.05 g) with varying molar  
 288 ratios were dispersed in Methylene Blue  
 289 solution (100 mL, 0.005 g/L) using  
 290 ultrasonication and subjected to visible light  
 291 irradiation for intervals of 20, 40, 60, 80, 100  
 292 and 120 minutes.  
 293

### 294 3 Results and Discussions

295  
 296 The XRD patterns shown in Fig. 1 display the  
 297 diffraction patterns of Fe<sub>3</sub>O<sub>4</sub>/ZnO/CuO  
 298 nanocomposites that were synthesized in  
 299 different molar ratios of CuO. The patterns  
 300 exhibit characteristic diffraction peaks  
 301 corresponding to cubic spinel Fe<sub>3</sub>O<sub>4</sub>,  
 302 monoclinic CuO, and hexagonal wurtzite ZnO  
 303 structures. The absence of any impurities or  
 304 secondary phases in the patterns demonstrates  
 305 that the Fe<sub>3</sub>O<sub>4</sub>/ZnO/CuO nanocomposites were  
 306 synthesized successfully. All XRD peaks  
 307 corresponding to [101] Planes related to

308 hexagonal ZnO structure (2 $\Theta$  =32.5), [200]  
 309 planes related to CuO monoclinic structure (2 $\Theta$   
 310 =39.5) and [311] planes for cubic spinel  
 311 structure Fe<sub>3</sub>O<sub>4</sub> (2 $\Theta$  =35.5) have the highest  
 312 growth rates. Furthermore, analysis of the XRD  
 313 patterns for Fe<sub>3</sub>O<sub>4</sub>/ZnO/CuO nanocomposites  
 314 with varying molar ratios reveals a clear trend:  
 315 as the molar ratio of CuO to ZnO increases,  
 316 there is a corresponding increase in the  
 317 intensity of CuO diffraction peaks, while  
 318 simultaneously showing a decrease in the  
 319 intensity of both ZnO and Fe<sub>3</sub>O<sub>4</sub> diffraction  
 320 peaks. Changes in the intensity of the pattern  
 321 revealed the increase of CuO content within  
 322 the nanocomposite structure.

323 In all XRD diagrams, considering the peak  
 324 positions, it can be seen that ZnO does not form  
 325 a solid solution with CuO and Fe<sub>3</sub>O<sub>4</sub>, and the  
 326 Fe<sub>3</sub>O<sub>4</sub>/ZnO/CuO nanocomposite is considered  
 327 as a nanocomposite powder of ZnO, Fe<sub>3</sub>O<sub>4</sub> and  
 328 CuO crystals.

329 Fig. 2 shows the XRD pattern of  
 330 Fe<sub>3</sub>O<sub>4</sub>/ZnO/CuO nanocomposite with molar  
 331 ratios of 1:1:0.3, 1:1:0.5, 1:1:1, and 1:1:3 for  
 332 a,b,c, and d images, respectively. According to  
 333 reference data, 01-075-0033 demonstrated  
 334 Fe<sub>3</sub>O<sub>4</sub> in the cubic phase, 0254-041-00  
 335 determined the hexagonal crystalline phase of  
 336 ZnO, and 0704-076-01 demonstrated CuO with  
 337 a monoclinic crystalline structure.

338 In Table. 1, the particle size of Fe<sub>3</sub>O<sub>4</sub>, ZnO,  
 339 CuO, and Fe<sub>3</sub>O<sub>4</sub>/ZnO/CuO nanocomposites  
 340 with molar ratios of 1:1:0.3, 1:1:0.5, 1:1:1 and  
 341 1:1:3 estimated by Scherrer's equation. By  
 342 comparing the size of Fe<sub>3</sub>O<sub>4</sub>, ZnO, and CuO  
 343 particles in Fe<sub>3</sub>O<sub>4</sub>/ZnO/CuO nanocomposites  
 344 with different molar ratios, it is observed that  
 345 the presence of CuO inhibits the growth of  
 346 particles and reduces the size of ZnO and Fe<sub>3</sub>O<sub>4</sub>  
 347 particles. In conclusion, CuO nanoparticles  
 348 inhibit the growth of ZnO crystallites. It was  
 349 evidenced by the significant reduction in ZnO  
 350 crystallite size in the presence of CuO. In  
 351 contrast, Fe<sub>3</sub>O<sub>4</sub> crystallite size shows a smaller

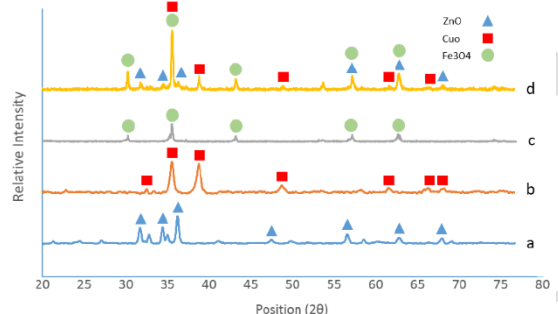
352 decrease, indicating that CuO has a less  
353 pronounced effect on the growth of  $\text{Fe}_3\text{O}_4$   
354 crystallites. The crystallite size of CuO varies  
355 depending on its concentration in the  
356 composites, highlighting its role in controlling  
357 crystallite growth in nanocomposites.

358 **Table1.** crystallite size of ZnO, CuO, and  $\text{Fe}_3\text{O}_4$  in  
359  $\text{Fe}_3\text{O}_4/\text{ZnO}/\text{CuO}$  nanocomposite

samples	ZnO crystallite size (nm)	CuO crystallite size (nm)	$\text{Fe}_3\text{O}_4$ crystallite size (nm)
$\text{Fe}_3\text{O}_4$	-	-	44.5
CuO	-	19.31	-
ZnO	22.92	-	-
$\text{Fe}_3\text{O}_4/\text{ZnO}/\text{CuO}(1:1:0.3)$	19.21	20.15	44.01
$\text{Fe}_3\text{O}_4/\text{ZnO}/\text{CuO}(1:1:0.5)$	20.18	16.15	42.23
$\text{Fe}_3\text{O}_4/\text{ZnO}/\text{CuO}(1:1:1)$	19.65	18.62	41.15
$\text{Fe}_3\text{O}_4/\text{ZnO}/\text{CuO}(1:1:3)$	17.15	21.48	40.15

3

361



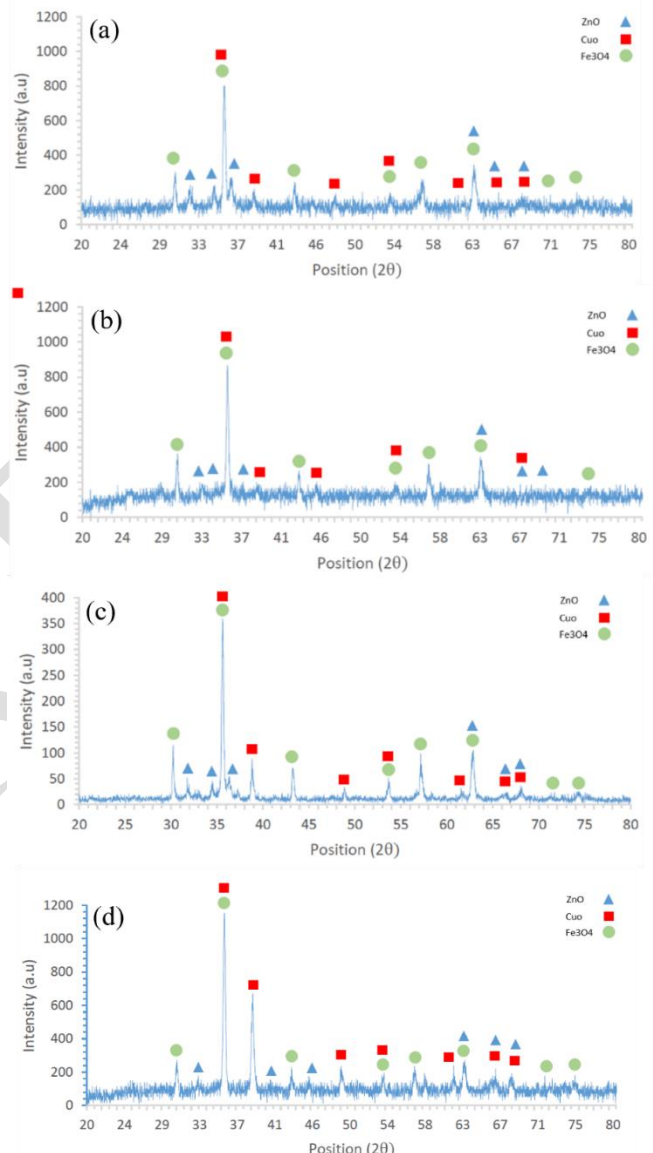
362

363 **Fig. 1.** XRD patterns of synthesized  
364  $\text{Fe}_3\text{O}_4/\text{ZnO}/\text{CuO}$  nanocomposite: (a) ZnO, (b)  
365 CuO, (c)  $\text{Fe}_3\text{O}_4$ , (d)  $\text{Fe}_3\text{O}_4/\text{ZnO}/\text{CuO}$   
366 nanocomposite.

367 Particle morphology of nanocomposites was  
368 investigated by scanning electron microscopy  
369 (SEM). Fig. 3 illustrates an SEM image of a  
370  $\text{Fe}_3\text{O}_4/\text{ZnO}/\text{CuO}$  nanocomposite with a molar  
371 ratio of 1:1:0.5. As shown in Fig.3, the  
372  $\text{Fe}_3\text{O}_4/\text{ZnO}/\text{CuO}$  nanocomposite is  
373 cauliflower-shaped. To compare the results, the  
374 size distribution of the conventional and  
375 synthesized catalysts was considered using  
376 ImageJ software. The analysis revealed that the  
377 synthesized samples exhibited relatively small  
378 average particle dimensions. This size  
379 distribution indicates the successful formation

381 of nanostructured materials. Similar  
382  $\text{Fe}_3\text{O}_4/\text{ZnO}/\text{CuO}$  morphologies have been  
383 reported in previous studies[20].

384



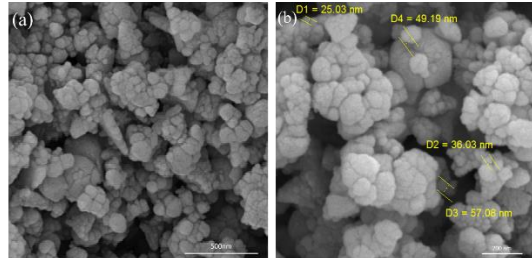
385 **Fig. 2.** XRD patterns of synthesized  
386  $\text{Fe}_3\text{O}_4/\text{ZnO}/\text{CuO}$  nanocomposite: (a)  
387  $\text{Fe}_3\text{O}_4/\text{ZnO}/\text{CuO}(1:1:0.3)$ ,  
388 (b)  $\text{Fe}_3\text{O}_4/\text{ZnO}/\text{CuO}(1:1:0.5)$ , (c)  $\text{Fe}_3\text{O}_4/\text{ZnO}/\text{CuO}$   
389 (1:1:1) and (d)  $\text{Fe}_3\text{O}_4/\text{ZnO}/\text{CuO}(1:1:3)$ .

391

392 Above all, the numerous pores of different  
393 sizes within the 3D microstructure act as  
394 transport pathways for small molecules. This  
395 morphology and porosity provide a larger  
396 surface area for dye adsorption and catalytic  
397 reactions. The reduction in particle dimensions

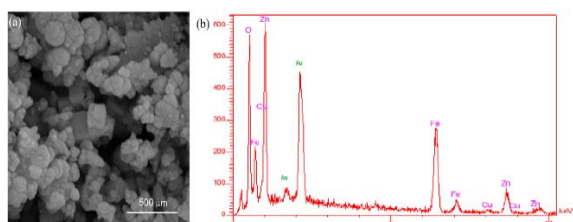
398 enhances the generation of electron-hole pairs  
 399 when exposed to light, resulting in more  
 400 effective degradation of contaminants during  
 401 performance testing.

402



403  
 404 **Fig. 3.** SEM image of synthesized  $\text{Fe}_3\text{O}_4/\text{ZnO}/\text{CuO}$   
 405 nanocomposite, (a)SEM Mag 70kx  
 406 (b) SEM Mag 100kx Particle Size Distribution  
 407

408 EDX analysis aims to define the dispersion of  
 409 the elements on the surface of the catalyst. As  
 410 shown in Fig. 4, the characteristic peaks of the  
 411 elements of oxygen, iron, copper, and zinc  
 412 indicate the presence of these elements in the  
 413 nanocomposite structure. It should be noted  
 414 that the samples had no impurities. The peak in  
 415 the range of 1.8 and 2.2 keV is related to the  
 416 gold element, covered on the nanocomposite in  
 417 SEM analysis, to provide conductivity in the  
 418 sample. Also in Table 2, the weight percentage  
 419 and atomic percentage of the elements are  
 420 specified, which proves the proper synthesis of  
 421 the samples.



422  
 423 **Fig. 4.** EDX analysis of synthesized  
 424  $\text{Fe}_3\text{O}_4/\text{ZnO}/\text{CuO}$  nanocomposite: (a) SEM image  
 425 of the area selected for EDX analysis, (b) EDX  
 426 results in  $\text{Fe}_3\text{O}_4/\text{ZnO}/\text{CuO}$  nanocomposite (1:1:0.5)

427

428

429

430

431 **Table 2.** Comparative amount of elements in the  
 432 structure of  $\text{Fe}_3\text{O}_4/\text{ZnO}/\text{CuO}$  nanocomposite  
 (1:1:0.5)

433

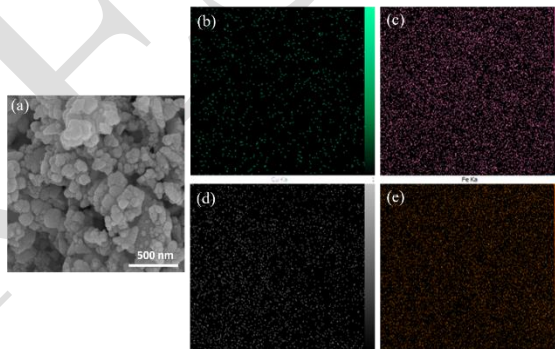
434

samples	Weight percentage (% W)	Atomic percentage (% A)
$\text{O}_{\text{K}\alpha}$	28.77	60.03
$\text{Cu}_{\text{K}\alpha}$	1.72	0.9
$\text{Zn}_{\text{K}\alpha}$	28.38	14.49
$\text{Fe}_{\text{K}\alpha}$	41.12	24.57

435

436

437 To investigate the distribution of elements in  
 438 the photocatalyst structure, dot Map analysis  
 439 was prepared from  $\text{Fe}_3\text{O}_4/\text{ZnO}/\text{CuO}$   
 440 nanocomposite (1:1:0.5) as shown in Fig. 5.  
 441 The elemental distribution analysis of the  
 442 photocatalyst structure was conducted on the  
 443 selected region shown in Fig. 5a. Images 5b,  
 444 5c, 5d, and 5e show the distribution of copper,  
 445 iron, zinc, and oxygen, respectively. Moreover,  
 446 the elements are homogeneously distributed in  
 447 the structure.



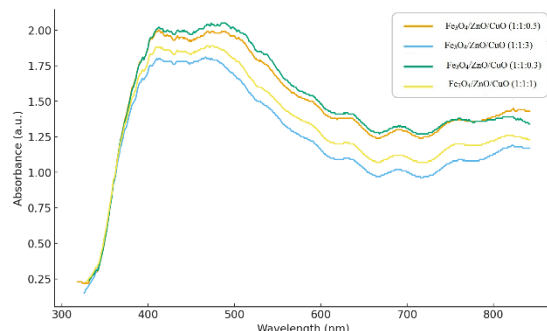
448  
 449 **Fig. 5.** Dot map analysis of synthesized  
 450  $\text{Fe}_3\text{O}_4/\text{ZnO}/\text{CuO}$  nanocomposite: (a) Selected area  
 451 for dot map analysis, (b) Cu, (c) Fe, (d) Zn, (e) O

452 In this study, the photocatalytic performance of  
 453  $\text{Fe}_3\text{O}_4/\text{ZnO}/\text{CuO}$  nanocomposites was  
 454 investigated by analyzing the relationship  
 455 between band gap and varying molar ratios of  
 456 the components. The photocatalytic  
 457 degradation efficiency of pollutants is  
 458 primarily determined by the band gap, which  
 459 serves as the critical parameter in the process.  
 460 For this purpose, the absorption spectrum of  
 461 nanocomposites was measured by a UV-visible  
 462 device, and the results are shown in Fig. 6(a).  
 463 The bandgap energies of the samples were  
 464 determined using Tauc's plots by extrapolating  
 465 the linear part of plots to the  $h\nu$  axis as shown  
 466 in Fig. 6 (b).

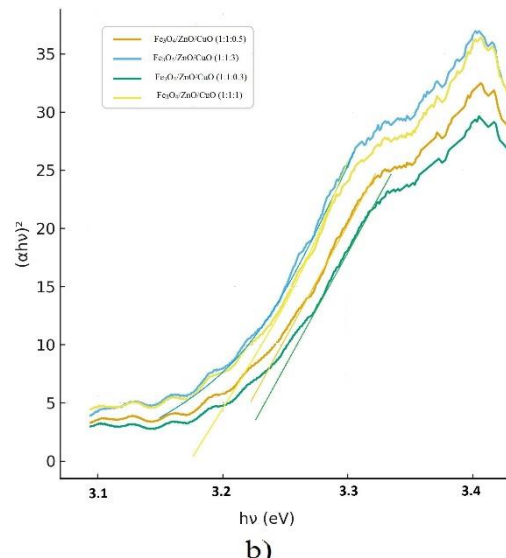
467  $\text{ZnO}$  nanoparticles exhibit strong absorption in  
 468 the wavelength range of 200-400 nm, and the

469 absorption edge of the samples shifts to 372 nm  
 470 with increasing copper oxide content in the  
 471 visible light region. Coupling zinc oxide with  
 472 copper oxide leads to a narrowing of the band  
 473 gap. This reduction in the band gap occurs  
 474 because the addition of copper oxide to the  
 475 nanocomposite introduces an intermediate  
 476 energy band at the bottom of the conduction  
 477 band of zinc oxide. This interaction decreases  
 478 the energy difference between the valence band  
 479 and the conduction band of zinc oxide, thereby  
 480 reducing the overall band gap energy.  
 481 According to the literature, ZnO nanoparticles  
 482 are n-type semiconductors, and the  
 483 semiconductor CuO nanoparticles are p-type.  
 484 In this study, the photocatalytic performance  
 485 was enhanced by creating a heterojunction  
 486 between n-type and p-type semiconductors,  
 487 while simultaneously studying how this  
 488 junction influences the optical characteristics.  
 489 In Table 3, the absorption wavelength and  
 490 energy of the band gap region for each sample  
 491 are calculated using the following equation:  
 492  $(\alpha h\nu)^2 = A(h\nu - E_g)$  (Eq.4)

493 where  $\alpha$  is the absorption coefficient,  $h$  is  
 494 Planck's constant,  $\nu$  is the photon frequency,  
 495  $E_g$  is the optical band gap, and  $A$  and  $n$  are  
 496 constants. For the direct bandgap  
 497 semiconductor,  $n = 2$ , and for the indirect  
 498 transition bandgap,  $n = 1/2$ . We assumed  $n = 2$  for  
 499 our samples.



a)



504  
 505 **Fig. 6.** Bandgap analysis curves of  $\text{Fe}_3\text{O}_4/\text{ZnO}/\text{CuO}$   
 506 nanocomposite: a) UV-VIS Absorption Spectra, b)  
 507 Tauc's plots graphs ( $n=2$ )  
 508  
 509  
 510

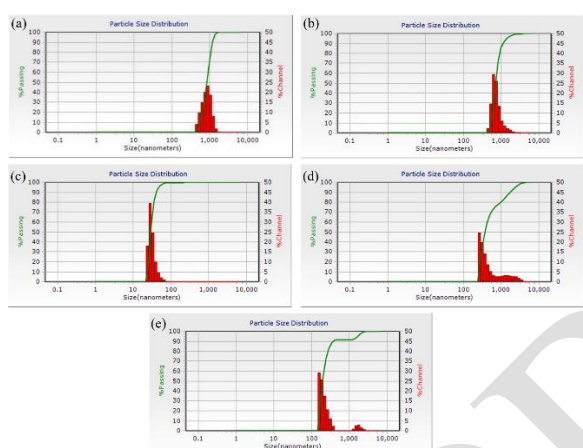
511 **Table 3.** Wavelength values of the absorption edge  
 512 and the energy of the band gap of ZnO and  
 513  $\text{Fe}_3\text{O}_4/\text{ZnO}/\text{CuO}$  nanocomposites

Samples	Wavelength of absorption edge (nm)	Energy of the band gap (eV)
ZnO	382.16	3.24
$\text{Fe}_3\text{O}_4/\text{ZnO}/\text{CuO}$ (1:1:0.3)	384.1	3.22
$\text{Fe}_3\text{O}_4/\text{ZnO}/\text{CuO}$ (1:1:0.5)	386.31	3.20
$\text{Fe}_3\text{O}_4/\text{ZnO}/\text{CuO}$ (1:1:1)	389.26	3.18
$\text{Fe}_3\text{O}_4/\text{ZnO}/\text{CuO}$ (1:1:3)	398.54	3.11

514  
 515  
 516 DLS analysis was performed to investigate  
 517 particle size distribution. Fig. 7 illustrates the  
 518 range of particle size distribution in the ZnO,  
 519  $\text{Fe}_3\text{O}_4/\text{ZnO}/\text{CuO}$ (1:1:0.3),  
 520  $\text{Fe}_3\text{O}_4/\text{ZnO}/\text{CuO}$ (1:1:0.5),  
 521  $\text{Fe}_3\text{O}_4/\text{ZnO}/\text{CuO}$ (1:1:1) and  
 522  $\text{Fe}_3\text{O}_4/\text{ZnO}/\text{CuO}$ (1:1:3) samples are 486-1944,  
 523 486-6540, 25-409, 289-6540, 171.9-6540 nm,  
 524 respectively.

525 On the other hand, the highest number of  
 526 particles in the ZnO,  $\text{Fe}_3\text{O}_4/\text{ZnO}/\text{CuO}$ (1:1:0.3),  
 527  $\text{Fe}_3\text{O}_4/\text{ZnO}/\text{CuO}$  (1:1:0.5),  $\text{Fe}_3\text{O}_4/\text{ZnO}/\text{CuO}$   
 528 (1:1:1), and  $\text{Fe}_3\text{O}_4/\text{ZnO}/\text{CuO}$  (1:1:3) samples  
 529 are 972, 687, 30.04, 289, and 171.9 nm,  
 530 respectively. DLS measures the hydrodynamic  
 531 diameter of particles (or agglomerates) in a  
 532 solution, which is typically much larger than

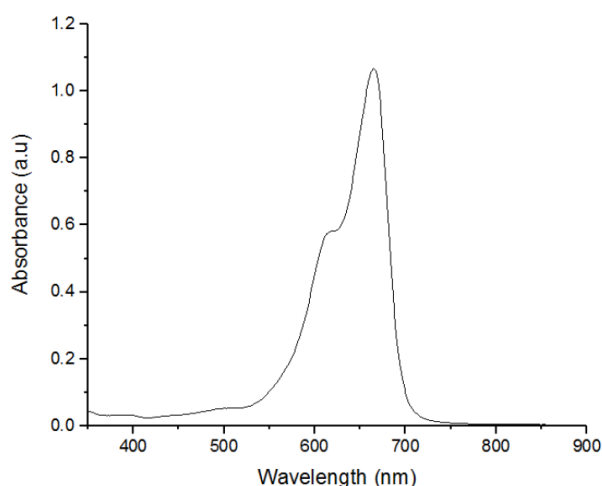
533 the primary particle size seen in SEM or the  
 534 crystallite size from XRD. The results show  
 535 that increasing the percentages of CuO in the  
 536  $\text{Fe}_3\text{O}_4/\text{ZnO}/\text{CuO}$  nanocomposite does not have  
 537 a steady effect on particle size. In general,  
 538 although the particle size in the nanocomposite  
 539 decreased compared to the particle size in pure  
 540  $\text{ZnO}$  samples but also the DLS data also  
 541 indicate severe agglomeration of the primary  
 542 nanoparticles in suspension, which is a critical  
 543 factor for photocatalytic performance as it  
 544 affects the active surface area.  
 545



546  
 547 **Fig. 7.** DLS Analysis Results of  $\text{Fe}_3\text{O}_4/\text{ZnO}/\text{CuO}$   
 548 nanocomposites, (a)  $\text{ZnO}$ , (b)  $\text{Fe}_3\text{O}_4/\text{ZnO}/\text{CuO}$   
 549 (1:1:0.3),  
 550 (c)  $\text{Fe}_3\text{O}_4/\text{ZnO}/\text{CuO}$  (1:1:0.5), (d)  $\text{Fe}_3\text{O}_4/\text{ZnO}/\text{CuO}$   
 551 (1:1:1), (e)  $\text{Fe}_3\text{O}_4/\text{ZnO}/\text{CuO}$  (1:1:3)  
 552

553 To investigate the various factors that affect the  
 554 photocatalytic properties, the  $\text{Fe}_3\text{O}_4/\text{ZnO}/\text{CuO}$   
 555 nanocomposites with different molar ratios in  
 556 MB solution were individually irradiated with  
 557 UV and visible waves at 20-40-60-80-100-120  
 558 minutes. Fig. 8 shows the absorption spectrum  
 559 of MB before photocatalytic activity. The  
 560 absorption rate of methylene blue is  
 561 approximately 1.067 at 665 nm. The reduction  
 562 of this amount in the presence of  
 563  $\text{Fe}_3\text{O}_4/\text{ZnO}/\text{CuO}$  nanocomposite and  $\text{ZnO}$   
 564 samples under visible and UV radiation reflects  
 565 the color of this industrial dye. It demonstrates  
 566 the ability of this nanocomposite to treat  
 567 industrial wastewater.  
 568

569

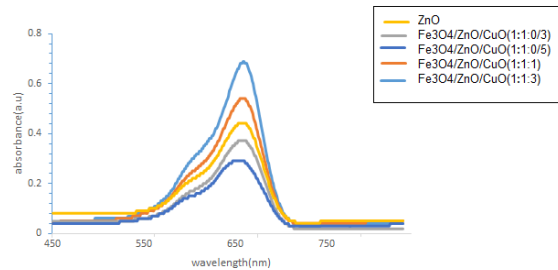


570  
 571 **Fig. 8.** Absorption spectrum of methylene blue  
 572 before photocatalytic activity.  
 573

574 Fig. 9 shows the results of the photocatalytic  
 575 activity under UV irradiation for over 120  
 576 minutes. The methylene blue absorption peak,  
 577 which had an initial concentration of 0.005 g /  
 578 L, decreased after 120 min in each sample. The  
 579 amount of methylene blue dye removal by the  
 580  $\text{Fe}_3\text{O}_4/\text{ZnO}/\text{CuO}$  samples with a molar ratio of  
 581 1:1:0.5 is higher than in other samples. The  
 582 photocatalytic activity of samples is  
 583 58.76%, 65.32%, 72.82%, 49.39%, and 35.33%  
 584 for  $\text{ZnO}$ ,  $\text{Fe}_3\text{O}_4/\text{ZnO}/\text{CuO}$  with the molar ratio  
 585 of 1:1:0.3, 1:1:0.5, 1:1:1, 1:1:3 respectively,  
 586 which were calculated using the formula.

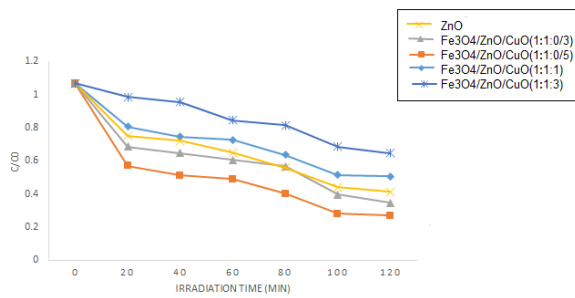
587 Fig. 10 illustrates a comparative diagram of the  
 588 photocatalytic performance of  $\text{Fe}_3\text{O}_4/\text{ZnO}/\text{CuO}$   
 589 nanocomposites with different amounts of CuO  
 590 under UV irradiation for 20 to 120 minutes.  
 591 Under UV irradiation,  $\text{Fe}_3\text{O}_4/\text{ZnO}/\text{CuO}$   
 592 nanocomposites with 1:1:1 and 1:1:3 molar  
 593 ratios have lower photocatalytic activity than  
 594 pure  $\text{ZnO}$ . The shift of the absorption edge  
 595 towards the visible spectrum and the reduction  
 596 in band gap of the nanocomposites can be  
 597 attributed to the incorporation of CuO. Due to  
 598 the differences between the UV wave energy  
 599 with the amount of energy which was needed  
 600 to transfer electrons from the valence band to  
 601 the conduction band in  $\text{Fe}_3\text{O}_4/\text{ZnO}/\text{CuO}$   
 602 nanocomposites, and the low efficiency of  
 603 electron-cavity generation compared to  $\text{ZnO}$ ,  
 604 the above nanocomposites exhibit less  
 605 photocatalytic activity.

606



607  
608 **Fig. 9.** Photocatalytic activity of  $\text{Fe}_3\text{O}_4/\text{ZnO}/\text{CuO}$   
609 nanocomposites under UV radiation.

610

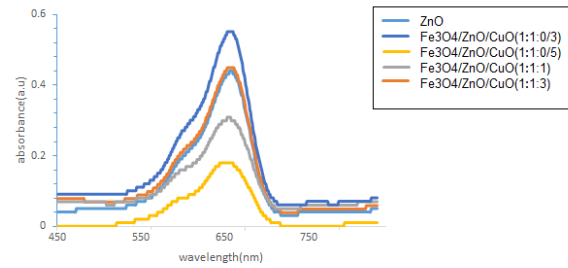


611  
612 **Fig. 10.** Comparative diagram of  $\text{Fe}_3\text{O}_4/\text{ZnO}/\text{CuO}$   
613 nanocomposites' photocatalytic efficiency under  
614 UV radiation.

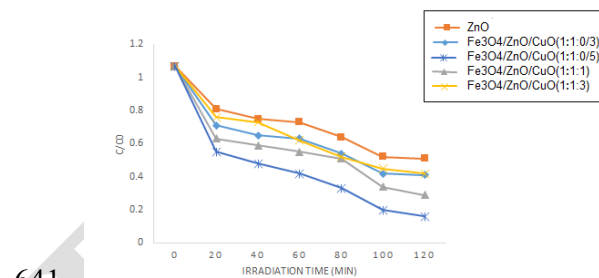
615

616 Fig. 11 shows the results of the photocatalytic  
617 activity under visible irradiation for over 120  
618 minutes. The  $\text{Fe}_3\text{O}_4/\text{ZnO}/\text{CuO}$  composite with  
619 a 1:1:0.5 molar ratio demonstrated superior  
620 methylene blue dye removal compared to other  
621 samples. The photocatalytic degradation  
622 efficiencies were measured at 48.45% for pure  
623  $\text{ZnO}$ , and for  $\text{Fe}_3\text{O}_4/\text{ZnO}/\text{CuO}$  composites:  
624 62.27% at 1:1:0.3 ratio, 88.7% at 1:1:0.5 ratio,  
625 77.94% at 1:1:1 ratio, and 57.82% at 1:1:3  
626 ratio. Fig. 12 shows a comparative diagram of  
627 the photocatalytic activity of  $\text{Fe}_3\text{O}_4/\text{ZnO}/\text{CuO}$   
628 nanocomposites with different amounts of  $\text{CuO}$   
629 under visible irradiation for 20 to 120 minutes.  
630 The  $\text{Fe}_3\text{O}_4/\text{ZnO}/\text{CuO}$  nanocomposite with a 1:  
631 1: 0.5 molar ratio exhibits the best  
632 photocatalytic activity. However, the  
633 photocatalytic activity of the samples improved  
634 concerning pure  $\text{ZnO}$ , indicating the higher  
635 photocatalytic activity of  $\text{Fe}_3\text{O}_4/\text{ZnO}/\text{CuO}$   
636 nanocomposites in the visible light range.

637



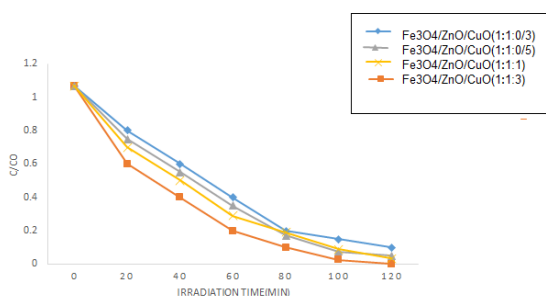
638  
639 **Fig. 11.** photocatalytic activity of  $\text{Fe}_3\text{O}_4/\text{ZnO}/\text{CuO}$   
640 nanocomposites under visible radiation.



641  
642 **Fig. 12.** Comparative diagram of photocatalytic  
643 efficiency of  $\text{Fe}_3\text{O}_4/\text{ZnO}/\text{CuO}$  nanocomposites  
644 under visible radiation.

645

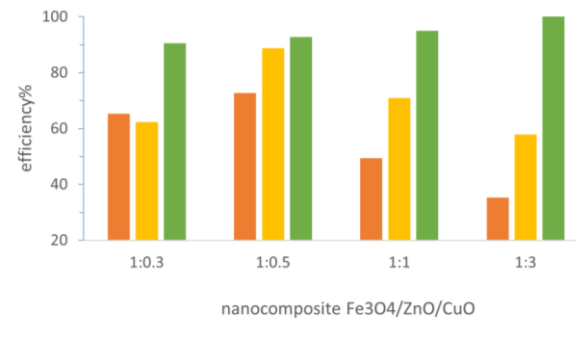
646 To investigate the influence of ultrasound on  
647 the photocatalytic activity of the  
648  $\text{Fe}_3\text{O}_4/\text{ZnO}/\text{CuO}$  nanocomposites with  
649 different molar ratios, the nanocomposites  
650 were irradiated with ultrasonic and visible light  
651 for 20-120 minutes in a methylene blue  
652 solution, and their photocatalytic activity was  
653 measured. Fig. 13 illustrates this. The results  
654 showed that the  $\text{Fe}_3\text{O}_4/\text{ZnO}/\text{CuO}$   
655 nanocomposites with the molar ratio of 1:13  
656 have the highest photocatalytic activity under  
657 ultrasound and visible light irradiation. The  
658 enhanced performance can be attributed to  
659  $\text{CuO}$ 's appropriate band gap characteristics.  
660 Under ultrasonic conditions,  $\text{CuO}$  showed  
661 higher activation compared to  $\text{ZnO}$ , and  
662 increasing the  $\text{CuO}$  content led to improved  
663 photocatalytic activity. As illustrated in Fig. 13,  
664 complete photocatalytic degradation (100%  
665 efficiency) was achieved after 120 minutes of  
666 treatment.



667  
668 **Fig. 13.** Comparative diagram of photocatalytic  
669 efficiency of Fe<sub>3</sub>O<sub>4</sub>/ZnO/CuO nanocomposites  
670 under visible and ultrasound radiation.

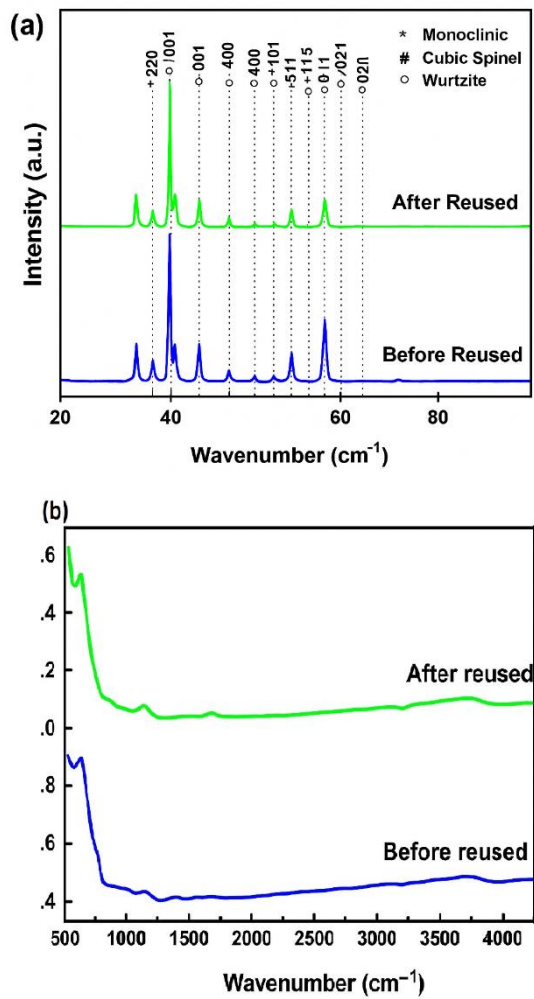
671 The Fe<sub>3</sub>O<sub>4</sub>/ZnO/CuO nanocomposites with  
672 different molar ratios were investigated under  
673 UV, visible, and ultrasonic waves, and their  
674 comparative results are shown in Fig. 14.  
675 Enhancing photocatalytic activity of the  
676 nanocomposite under visible light and  
677 ultrasonic by increasing CuO content is mainly  
678 attributed to the narrow band gap of CuO,  
679 which enables strong visible-light absorption  
680 and promotes efficient charge separation  
681 through the formation of the n-p  
682 heterojunction. In this procedure, CuO acts as  
683 an effective electron trap, repressing  
684 recombination and enhancing the generation of  
685 reactive species. Under ultrasonic-visible light,  
686 the highest efficiency was observed, which can  
687 be driven by two reasons. Firstly, Ultrasonic  
688 increases the production of active radicals for  
689 photocatalytic activity, and also improves the  
690 organic transfer of color between the catalyst  
691 surface. secondly, the de-agglomeration of  
692 photocatalysis particles by ultrasonication  
693 leads to an increase in the specific surface area.  
694 The ultrasonic process operates through  
695 cavitation that forms holes, leading to elevated

696 temperature and pressure conditions in the  
697 reaction medium. This process involves the  
698 formation, gradual growth, and eventual  
699 bursting of a series of bubbles by sonication.  
700 Under such conditions, hot spots are created  
701 that can convert water molecules into active  
702 hydroxyl radicals and hydrogen peroxide, and  
703 these active radicals destroy toxic compounds.



704  
705 **Fig. 14.** Comparative diagram of photocatalytic  
706 efficiency of Fe<sub>3</sub>O<sub>4</sub>/ZnO/CuO nanocomposites  
707 under UV, visible, and ultrasonic radiation.  
708  
709

710 Based on other related research, stability of  
711 the catalysts under light and ultrasonic  
712 irradiation was evaluated by the same batch of  
713 nanocomposites for four cycles, with the same  
714 amount of fresh MB solutions added after each  
715 run. The results in Fig. 15 show that the  
716 catalysts exhibit good stability and magnetic  
717 recyclability from the treated solutions after  
718 successive degradation reactions.  
719 The XRD and FTIR measurements were also  
720 performed on the catalysts after multiple  
721 cycles, and compared with the results obtained  
722 before the reaction. In Fig. 15(a), all XRD peaks  
723 corresponding to cubic spinel, hexagonal  
724 wurtzite, and monoclinic structures remained at  
725 the same values after four cycles. So, there is  
726 no change in the crystalline structure.  
727 The same conclusion is drawn from the IR  
728 absorption measurements because the IR peaks  
729 of the functional groups remain unchanged  
730 after photocatalytic degradation, Fig. 15(b)  
731 [30].



732

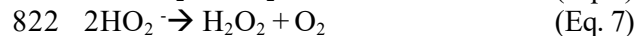
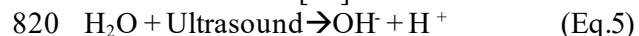
733 **Fig. 15.** a) XRD patterns of  $\text{Fe}_3\text{O}_4/\text{ZnO}/\text{CuO}$   
 734 nanocomposites after and before reused,b) IR  
 735 peaks of  $\text{Fe}_3\text{O}_4/\text{ZnO}/\text{CuO}$  nanocomposites after  
 736 and before reused [30]

737

738 Various factors such as the generation, trapping  
 739 of electrons, charge carrier recombination, the  
 740 average size of the crystals, and the energy of  
 741 the band gap, are important factors that we can  
 742 propose the mechanism of the photocatalyst.  
 743 The varying molar proportions of CuO in the  
 744 samples significantly influence the  
 745 photocatalytic mechanism. Research has  
 746 shown that a larger specific surface area creates  
 747 more active surface sites, which reduces the  
 748 interfacial charge carrier transfer resistance and  
 749 enhances photocatalytic performance. The  
 750 nanocomposites show different patterns of  
 751 photocatalytic performance when exposed to  
 752 visible light versus UV radiation.

753 The diffuse reflectance spectroscopy analysis  
 754 revealed that ZnO has a band gap of 3.24 eV,  
 755 while CuO exhibits a band gap of 1.54 eV[30].  
 756 As an n-type semiconductor, ZnO's electrons in  
 757 the valence band become excited and move to  
 758 the conduction band when exposed to UV  
 759 radiation, which is possible due to its specific  
 760 band gap energy. In contrast, CuO, being a p-  
 761 type semiconductor, can achieve electron  
 762 transfer from the valence to the conduction  
 763 band through visible light exposure. The  
 764 complementary band gap energies of ZnO,  
 765 CuO, and  $\text{Fe}_3\text{O}_4$  can enhance electron transfer  
 766 between these materials. When exposed to  
 767 visible light, CuO generates electron-hole pairs  
 768 because of its favorable band gap.  
 769 Additionally, electrons from ZnO's valence  
 770 band, which possess lower energy compared to  
 771 its conduction band, can move into structural  
 772 defects like oxygen vacancies. When CuO's  
 773 excited electrons migrate to ZnO's conduction  
 774 band, they can interact with  $\text{Fe}^{3+}$  to form  $\text{Fe}^{2+}$   
 775 ions. These unstable  $\text{Fe}^{2+}$  ions then react with  
 776 oxygen molecules to generate superoxide  
 777 radicals. Simultaneously, holes created in  
 778 ZnO's valence band can either transfer to CuO's  
 779 valence band or interact with water molecules  
 780 to create  $\text{OH}^-$ . Additionally, holes in CuO can  
 781 also generate hydroxyl radicals through water  
 782 interaction. Under UV light, the capture of  
 783 electrons by  $\text{Fe}^{3+}$  ions enhances the probability  
 784 of hole-mediated hydroxyl radical formation,  
 785 which then breaks down organic pollutants.  
 786 During this process, electrons from ZnO's  
 787 valence band are exclusively excited to its  
 788 conduction band, creating holes in the valence  
 789 band. These excited electrons are captured by  
 790  $\text{Fe}^{3+}$  ions, forming  $\text{Fe}^{2+}$  ions that produce  
 791 superoxide radicals. Concurrently, the  
 792 photogenerated holes react with water  
 793 molecules to form  $\text{OH}^-$  radicals, which are the  
 794 key agents in decomposing methylene blue  
 795 during the catalytic reaction [26-28].  
 796 The mechanism behind MB degradation using  
 797 ultrasonic treatment has been verified. When  
 798 ultrasonic waves are applied, they induce  
 799 acoustic cavitation, generating extreme  
 800 conditions of temperature (5000 K) and  
 801 pressure (1000 atm). This process produces  
 802 light across a broad wavelength spectrum  
 803 (sonoluminescence), activating both ZnO and

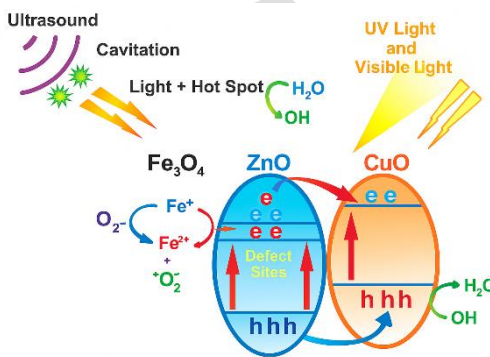
804 CuO semiconductors and forming electron-  
 805 hole pairs [28]. These electron-hole pairs  
 806 contribute to MB degradation through the same  
 807 mechanisms observed in photocatalysis. When  
 808 exposed to both visible light and ultrasound,  
 809 CuO shows enhanced activation due to its  
 810 suitable band gap energy. This explains why  
 811 the nanocomposite containing the highest  
 812 proportion of CuO ( $\text{Fe}_3\text{O}_4/\text{ZnO}/\text{CuO}$  in a 1:1:3  
 813 molar ratio) demonstrates superior  
 814 photosonocatalytic performance under visible  
 815 light conditions. Moreover, the extreme  
 816 temperature and pressure conditions created by  
 817 ultrasound in aqueous environments promote  
 818 the direct formation of  $\text{OH}^-$  radicals through  
 819 Fenton reactions [29]:



824 According to Yuan and colleagues' research  
 825 [30], the  $\text{H}_2\text{O}_2$  produced (as shown in Eq. 7) can  
 826 interact with  $\text{Fe}^{2+}$  to generate  $\text{OH}^-$  radicals and  
 827  $\text{Fe}^{3+}$  ions. The increased production of  $\text{OH}^-$   
 828 radicals through various pathways under  
 829 ultrasonic irradiation results in improved  
 830 degradation efficiency.

831 The reason that the ternary nanocomposite with  
 832 the ratio of 1:1:0.5 is optimal under visible  
 833 light, while 1:1:3 is best under sonolysis, is  
 834 attributed to the narrow band gap of CuO,  
 835 which enables strong visible-light absorption  
 836 and promotes efficient charge separation  
 837 through the formation of the n-p  
 838 heterojunction. In this procedure, CuO acts as  
 839 an effective electron trap, repressing  
 840 recombination and enhancing the generation of  
 841 reactive species. In contrast, under UV  
 842 irradiation, increasing the ratio of CuO in the  
 843 nanocomposite reduces the photocatalytic  
 844 performance because CuO does not absorb UV  
 845 efficiently and partially covers the surface of  
 846 the primary semiconductor (reducing the

847 specific interface areas). Also, agglomeration  
 848 occurs by increasing CuO content, which limits  
 849 the UV absorption. Moreover, extra CuO can  
 850 behave as recombination centers, accelerating  
 851 electron-hole recombination and lowering the  
 852 overall photocatalytic activity.



853  
 854 **Fig. 16.** Schematic of the photocatalytic  
 855 mechanism of  $\text{Fe}_3\text{O}_4/\text{ZnO}/\text{CuO}$  nanocomposites

#### 856 **4 Conclusions**

857 In conclusion, the  $\text{Fe}_3\text{O}_4/\text{ZnO}/\text{CuO}$   
 858 nanocomposites were successfully produced  
 859 using the sol-gel synthesis technique. The  
 860 degradation of methylene blue was examined  
 861 under both light and ultrasonic irradiation to  
 862 analyse the photocatalytic activity. Results  
 863 revealed that ultrasonic treatment played a  
 864 crucial role and significantly improved the  
 865 photocatalytic performance of the  
 866 nanocomposite materials. The optimal  
 867 composition of the photocatalyst  
 868 nanocomposite material was investigated  
 869 through structural characterization using  
 870 various techniques. SEM images shown that  
 871 the nanocomposite exhibited a cauliflower-like  
 872 structure with particle size distribution ranging  
 873 from 25.3 to 57.08 nm, as measured by ImageJ  
 874 software. EDX analysis also confirmed  
 875 improved dispersion of the samples.  
 876 Additionally, dot mapping of the  
 877 nanocomposite structure indicated that the  
 878 elements were uniformly distributed  
 879 throughout the material. Dynamic Light  
 880 Scattering (DLS) results showed that  
 881 increasing the copper oxide content in the  
 882  $\text{Fe}_3\text{O}_4/\text{ZnO}/\text{CuO}$  nanocomposite led to a  
 883 reduction in particle size distribution.

884 Moreover, the addition of CuO decreased the  
 885 band gap energy, shifting light absorption  
 886 toward the visible region. The photocatalytic  
 887 performance revealed 100% degradation of  
 888 MB for  $\text{Fe}_3\text{O}_4/\text{ZnO}/\text{CuO}$  nanocomposite at a  
 889 1:1:3 molar ratio under ultrasound and visible  
 890 light after 120 minutes. Additionally, the use of  
 891 an external magnet allowed for easy separation  
 892 and recovery of the nanocomposite from the  
 893 solution after the reaction. These findings  
 894 highlight the effectiveness of the ternary  
 895  $\text{Fe}_3\text{O}_4/\text{ZnO}/\text{CuO}$  nanocomposite catalyst in  
 896 removing organic pollutants from wastewater.  
 897

## Acknowledgements

898 The authors gratefully acknowledge the  
 899 mechanical faculty of Tabriz University and  
 900 the laboratory of the Materials Science and  
 901 Engineering Department of Tabriz University.  
 903

## 904 References

- 905 1. Zhu, L.; Zhou, Y.; Fei, L.; Cheng, X.;  
 906 Zhu, X.; Deng, L.; Ma, X. "Z-scheme  
 907  $\text{CuO}/\text{Fe}_3\text{O}_4/\text{GO}$  heterojunction  
 908 photocatalyst: Enhanced  
 909 photocatalytic performance for  
 910 elimination of tetracycline." *Chemosphere* 2022, 309 (Pt 2),  
 911 136721.
- 913 2. Alzuabidi, H. A.; Naghipour, A.;  
 914 Fardood, S. T. "Green synthesis and  
 915 characterization of  $\text{Cu}_{0.5}\text{Zn}_{0.5}\text{FeAlO}_4$   
 916 magnetic nanoparticles with enhanced  
 917 photocatalytic activity." *J. Ultrafine  
 918 Grained Nanostruct. Mater.* 2024,  
 919 158–167.
- 920 3. Hu, Y.; Jensen, L.; Schatz, G.  
 921 "Photocatalytic reaction pathways on  
 922  $\text{TiO}_2$  surfaces: a theoretical study." *J.  
 923 Am. Chem. Soc.* 2006, 128, 15734–42.
- 924 4. Ge, M.; Cao, C.; Huang, J.; Li, S.;  
 925 Chen, Z.; Zhang, K.; et al. "A review  
 926 of one-dimensional  $\text{TiO}_2$   
 927 nanostructured materials for  
 928 environmental and energy
- 929 5. Asghar, A.; Aziz, A.; Mohd, A.  
 930 "Advanced oxidation processes for in  
 931 situ production of hydrogen  
 932 peroxide/hydroxyl radical for textile  
 933 wastewater treatment: a review." *J.  
 934 Cleaner Prod.* 2015, 87, 826–38.
- 935 6. Shakir, A. K.; Ghanbari-Adivi, E.;  
 936 Baron, A. S.; Soltani, M.  
 937 "Investigation of the Effect of  
 938 Calcination Time on the Antibacterial,  
 939 Antifungal and Anticancer Activities  
 940 of  $\text{TiO}_2/\text{ZnO}$  Nanocomposites." *Iran.  
 941 J. Mater. Sci. Eng.* 2025, 22 (1).
- 942 7. Safavi, M. S.; Bozorg, S.; Ahadzadeh,  
 943 I.; Safavi, M. S. "Development of  
 944 heterogeneous nano-zeolite catalyzing  
 945 Fenton-like oxidation processes for  
 946 metalworking fluid wastewater  
 947 treatment: A comparison with  
 948 conventional methods." *J. Ultrafine  
 949 Grained Nanostruct. Mater.* 2024,  
 950 190–202.
- 951 8. Asai, M. M.; Tapadia, K.  
 952 "Biofabricated magnetic  $\text{CuO}/\text{Fe}_3\text{O}_4$   
 953 nanocomposites: Synthesis,  
 954 characterization and Brilliant Green  
 955 dye removal from aqueous media and  
 956 its kinetics study." *J. Indian Chem.  
 957 Soc.* 2025, 102 (5), 10166.
- 958 9. Ajmal, A.; Majeed, I.; Malik, R.;  
 959 Idriss, H.; Nadeem, M. "Principles and  
 960 mechanisms of photocatalytic dye  
 961 degradation on  $\text{TiO}_2$ -based  
 962 photocatalysts: a comparative  
 963 overview." *RSC Adv.* 2014, 4, 37003–  
 964 26.
- 965 10. Soleimani-Amiri, S.; Hossaini, Z.;  
 966 Azizi, Z. "Synthesis and investigation  
 967 of biological activity of new  
 968 oxazinoazepines: Application of  
 969  $\text{Fe}_3\text{O}_4/\text{CuO}/\text{ZnO}/\text{MWCNT}$  magnetic  
 970 nanocomposite in reduction of 4-
- 971 972

applications." *Mater. Chem. A* 2016, 4, 6772–6801.



1060 *Applications*; 2019; Chapter 5, pp 121–  
1061 132.

1062 24. Chen, X.; Selloni, A. "Introduction:  
1063 Titanium dioxide ( $TiO_2$ )  
1064 nanomaterials." *Chem. Rev.* 2014, **114**,  
1065 9281–82.

1066 25. Etay, H.; Kumar, A.; Yadav, O. P.  
1067 "Kinetics of photocatalytic  
1068 degradation of methylene blue dye in  
1069 aqueous medium using  $ZnO$   
1070 nanoparticles under UV radiation." *J.  
1071 Anal. Pharm. Res.* 2023, **12** (1).

1072 26. Asli, S. A.; Taghizadeh, M.  
1073 "Sonophotocatalytic degradation of  
1074 pollutants by  $ZnO$ -based catalysts: A  
1075 review." *Chem. Select* 2020, 13720–  
1076 73.

1077 27. Benamara, M.; Nassar, K. I.; Essid, M.;  
1078 Frick, S.; Rugmini, R.; Sekhar, K. C.;  
1079 Silva, J. P. "Visible light-driven  
1080 removal of Rhodamine B using  
1081 indium-doped zinc oxide prepared by  
1082 sol–gel method." *J. Sol-Gel Sci.  
1083 Technol.* 2024, **111** (2), 553–65.

1084 28. Yuan, N.; Zhang, G.; Guo, S.; Wan, Z.  
1085 "Enhanced ultrasound-assisted  
1086 degradation of methyl orange and  
1087 metronidazole by rectorite-supported  
1088 nanoscale zero-valent iron." *Ultrason.  
1089 Sonochem.* 2016, **28**, 62.

1090 29. Khan, M. A. N.; Siddique, M.; Wahid,  
1091 F.; Khan, R. "Removal of reactive blue  
1092 19 dye by sono, photo and  
1093 sonophotocatalytic oxidation using  
1094 visible light." *Ultrason. Sonochem.*  
1095 2015, **26**, 370–77.

1096 30. Taufik, A.; Saleh, R. "Synthesis of iron  
1097 (II, III) oxide/zinc oxide/copper (II)  
1098 oxide( $Fe_3O_4/ZnO/CuO$ )  
1099 nanocomposites and their  
1100 photosonocatalytic property for  
1101 organic dye removal." *J. Colloid  
1102 Interface Sci.* 2017, **491**, 27–36.